

NEAR FIELD IMAGE RECONSTRUCTION ALGORITHM FOR PASSIVE MILLIMETER-WAVE IMAGER BHU-2D-U

Xianxun Yao*, Cheng Zheng, Jin Zhang, Baohua Yang, Anyong Hu, and Jungang Miao

School of Electronic and Information Engineering, Beihang University, Xueyuan Road 37th, Haidian District, Beijing 100191, China

Abstract—A passive millimeter-wave imager BHU-2D-U based on synthetic aperture interferometric radiometer (SAIR) technique has been developed by Beihang University. The imager is designed for detecting concealed weapons on human body and operated under the near-field condition of the antenna array, thus the conventional Fourier imaging theory does not apply. In this paper, an accurate numerical image reconstruction algorithm using regularization theory is proposed. By means of adding *a priori* information of desired brightness temperature image, the influences of measurement noise and focusing error on the reconstructed image have been reduced. Numerical simulations and experiments on BHU-2D-U have been performed to verify the superiorities of the proposed algorithm over the corrected Fourier method and the Moore-Penrose pseudo inverse method. The results demonstrate that the proposed method is an advantageous imaging algorithm for near-field millimeter-wave SAIR.

1. INTRODUCTION

Passive millimeter-wave imagers have become popular for high resolution observation of concealed weapons detection applications [1–5]. Compared with X-ray or radar instruments, passive imagers receive spontaneous radiations emitted or reflected by the interested subjects. Therefore, passive imagers are more appropriated if considering the human health issues. The Synthetic Aperture interferometric radiometer has been proved effective and capable of delivering high

Received 22 September 2013, Accepted 21 October 2013, Scheduled 22 October 2013

* Corresponding author: Xianxun Yao (yaoxianxun@ee.buaa.edu.cn).

spatial resolution over large field of view (FOV) required in the security applications.

A two-dimensional SAIR imager BHU-2D-U has been developed at Beihang University with an imaging distance about 3 m [6], which is operated under the near-field condition of the utilized antenna array. Thus, the Fourier imaging theory generally employed in the interferometry and radio astronomy applications does not apply any longer. To solve this problem, two methods have been reported: Corrected Fourier method introducing correction phase terms is able to provide accurate results by assuming point source condition but not for the cases of extended targets [7–9]. The alternative imaging method on the basis of Moore-Penrose pseudo inverse algorithm has been verified for the one-dimensional SAIR [10, 11]. However, the image reconstruction problem is not well-posed, when the large number of antennas and large FOV are applied. The ill-posed problem indicates that small focusing error and measurement noise in actual instrument can lead to large distortions in the reconstructed image. To reduce the errors in the reconstructed image, this paper presents a numerical imaging algorithm, which regularizes the problem with the aid of *a priori* information of the desired solution [12, 13].

In this paper, the near-field imaging principle of SAIR is reviewed, which indicates the unavailability to reconstruct brightness temperature image from near-field visibility function analytically. To solve the problem, a numerical imaging method is proposed by referring to the physical property of desired brightness temperature distribution and the regularization theory, which results smaller errors in the reconstructed image. To support the theoretical analysis, numerical simulations and experiments are carried out based on BHU-2D-U. The results verify the advantageous of the proposed algorithm for near-field millimeter-wave SAIR.

2. NEAR-FIELD IMAGING PRINCIPLE AND PROPOSED IMAGE RECONSTRUCTION ALGORITHM

2.1. The Visibility Function

The principle of SAIR is to measure the spectral components of the brightness temperature distribution in the FOV by correlating signals that are received by the antennas arranged in a plane, as is illustrated in Figure 1.

The observation antennas are located on the plane $z = 0$, while an extended source is located on plane $z = Z_0$. The visibility function

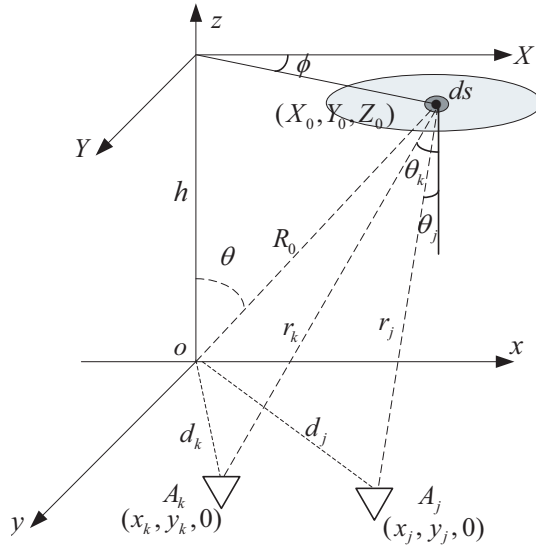


Figure 1. Near-field geometry diagram of 2-D SAIR measurement.

for any two antennas labeled k and j can be expressed as [14]

$$\begin{aligned}
 V_{kj}^N = & \frac{1}{\sqrt{\Omega_k \Omega_j}} \iint_{\text{source}} \frac{T(\theta, \phi)}{r_k r_j} F_{nk}(\theta_k, \phi_k) \\
 & \cdot F_{nj}^*(\theta_j, \phi_j) \tilde{r}_{kj} \left(\frac{r_k - r_j}{c} \right) e^{jk_0(r_k - r_j)} ds \quad (1)
 \end{aligned}$$

where the integral is extended over the source surface, T the brightness temperature of the target, and k_0 the wave number. $\Omega_{k,j}$ are the antennas equivalent solid angles, $r_{k,j}$ the distances between the source and observation elements, and $F_{nk,j}$ the normalized radiation voltage patterns of the antennas, which observe the image from their own coordinate system. $\tilde{r}_{ij}(\tau)$ is the fringe washing function (FWF), which accounts for spatial decorrelation effects. For ideal narrow-band imaging, the FWF can be neglected. The visibility function mainly depends on the path length difference $\Delta r = r_k - r_j$. According to the Figure 1, the distance r_k can be expressed as

$$r_k = \sqrt{(x_k - X_0)^2 + (y_k - Y_0)^2 + Z_0^2} \quad (2)$$

When $R_0 \gg d_{k,j}$, a linear Taylor approximation can be done and yields

$$\bar{r}_k = R_0 + \frac{d_k^2}{2R_0} - (\xi x_k + \eta y_k) \quad (3)$$

where $\xi = X_0/R_0$ and $\eta = Y_0/R_0$ are the direction cosines. Using the same equation for r_j , the phase difference $k_0\Delta\bar{r}$ can be written as

$$k_0\Delta\bar{r} = \bar{r}_k - \bar{r}_j = \varphi(u, v) - 2\pi(u\xi + v\eta) \quad (4)$$

where $\varphi(u, v) = \pi(d_k^2 - d_j^2)/R_0$, and $u = (x_k - x_j)/\lambda$ and $v = (y_k - y_j)/\lambda$ are called the baseline. In the case of far-field observation, the approximations, $\theta_k \approx \theta_j \approx \theta$, $r_k \approx r_j \approx r$, $\varphi_{k,j} \approx 0$ can be applied. In the case, the far-field visibility function can be expressed as

$$V_{kj}^F(u, v) = \iint_{\xi^2 + \eta^2 \leq 1} T_M(\xi, \eta) e^{-j2\pi(u\xi + v\eta)} d\xi d\eta \quad (5)$$

where

$$T_M(\xi, \eta) = \frac{T_B(\xi, \eta) F_{nk}(\xi, \eta) F_{nj}^*(\xi, \eta)}{\sqrt{1 - \xi^2 - \eta^2} \sqrt{\Omega_k \Omega_j}} \quad (6)$$

is the modified brightness temperature. It can be seen that the far-field visibility function is the inverse Fourier transforms of modified brightness temperature.

For near-field application, the linear Taylor approximation of Equation (3) will result in large approximation errors that indicate the direct Fourier theory is not suited for. To solve the problem, the corrected Fourier method can be employed to correct the near-field visibility measurement of Equation (1) by subtracting the near-field phase and adding the far-field phase [9]

$$V_{kj}^F = V_{kj}^N e^{-jk_0(r_k - r_j)} e^{-j2\pi(u\xi + v\eta)} \quad (7)$$

The method is fitted for the point source target, while the integration of Equation (1) is removed. However, for an extended source target, the near-field visibility function is not only determined by the different baseline, but also depended on the different location of the pixel point. In this case, the near-field visibility function just can be partially corrected by focusing the near-field visibility to one pixel in the FOV. The residual near-field model error cannot be avoided when the large FOV is required. Moreover, the spatial misalignments due to non-ideal installation of antennas are not considered in the method.

2.2. The Proposed Imaging Method

As analyzed in the previous section, it is impossible to correct the near-field visibility function to the far-field case. Considering the

finite resolution of the reconstructed image, the visibility function integral (1) can be discretized into a linear system of matrix equations

$$V_{kj} = \sum_p \sum_q \frac{T(\theta_{pq}, \phi_{pq})}{r_{k,pq} r_{j,pq} \sqrt{\Omega_k \Omega_j}} F_{nk}(\theta_{pq}, \phi_{pq}) \cdot F_{nj}^*(\theta_{pq}, \phi_{pq}) \tilde{r}_{kj} \left(\frac{\Delta r_{kj,pq}}{c} \right) e^{jk_B \Delta r_{kj} \Delta s} \quad (8)$$

Here numerical quadrature is used to represent integral Equation (1) as a summation over $p \times q$ integrand samples. By mapping (k, j) into single ones M and mapping (p, q) into single ones P , all of visibility samples can be written simultaneously as

$$V_{M \times 1} = G_{M \times P} \cdot T_{P \times 1} \quad (9)$$

where $V_{M \times 1}$ is the measured near-field visibility samples, $T_{P \times 1}$ the temperature matrix, $G_{M \times P}$ the system response matrix, and M the number of visibility samples including redundant ones. Since the redundant pairs of antennas in far field may lead to the different visibility samples in near field. P is the number of pixels in the brightness temperature distribution. In this case, the near-field image can be accurately reconstructed by means of numerical solution method.

For BHU-2D-U, the background cancelation technique has been used to reduce the influences of aliasing error and system offset [5, 6]. Thus the visibility function samples need to be pre-processed before image reconstruction

$$V' = V_{t+b_0} - V_{b+b_0} = G [T_{t+t_0} - T_{b+b_0}] = GT' \quad (10)$$

where V_{t+b_0} is the visibility sample of the target T_{t+b_0} , V_{b+b_0} the visibility sample of background T_{b+b_0} without the target, and T' describes the differential temperature distribution of the target. For BHU-2D-U, 4608 pixels ($P = 96 \times 48$) are used to satisfy the Nyquist sampling criteria and to make the numerical quadrature sufficiently accurate, while the number of complex visibility samples is $M = 48 \cdot (48 - 1)/2 = 1128$. Hence the matrix Equation (10) is underdetermined and the inverse problem does not usually have a straightforward solution. For ideal SAIR with a small array, the matrix G is generally well conditioned, and the Moore-Penrose pseudo inverse method can be used to get a stable solution [10]

$$T' = G^T (GG^T)^{-1} V' \quad (11)$$

where T denotes conjugate transpose operation, However, the large antenna array in BHU-2D-U results in the ill condition of matrix G . Moreover, considering the measurement noise and focusing error in

measured visibility samples, the direct problem of Equation (10) can be formulated as

$$V' + \Delta V' = (G + \Delta G) \cdot (T' + \Delta T') \quad (12)$$

Under this condition, the solution will be potentially very sensitive to the inevitable measurement errors in the visibility samples.

$$\frac{\|\Delta T'\|}{\|T'\|} \leq \frac{c(G)}{1 - c(G) \frac{\|\Delta G\|}{\|G\|}} \left(\frac{\|\Delta G\|}{\|G\|} + \frac{\|\Delta V'\|}{\|V'\|} \right) \quad (13)$$

where $c(G)$ is the condition number of G , which characterizes the posedness of the matrix equation. It has been found that the condition number of G increases with larger FOV and increasing number of antennas. Therefore, the inverse problem of BHU-2D-U is not well-posed. In this case, it is necessary to add *prior* information about the desired solution in order to suppress the propagation of errors from measured visibility samples to brightness temperature distribution and signal out a useful and stable solution.

In order to incorporate the further information about the desired solution, the physical property of the expected brightness temperature is taken into account. Firstly, the object workspace E' is defined as the space of the whole FOV, while the workspace E'' is the space of the target region $D(t)$ inside FOV (a subspace of E'). From Equation (10), the desired brightness temperature T' is equal to 0 outside the target region. Thus an operator R can be defined as

$$\begin{aligned} R : E' &\rightarrow E'' \\ T' &\rightarrow RT' = T'' \end{aligned}$$

With $\forall T' \in E'$

$$T'' = \begin{cases} T', & (\theta, \phi) \in D(t) \\ 0, & \text{otherwise} \end{cases} \quad (14)$$

where R is a $Q \times P$ matrix. Q is the number of pixels within the target region, while P is the number of pixels in the whole FOV. By the action of the operator, the dimension of desired solution T'' is reduced. The location and lineament of target region can be roughly estimated by the corrected Fourier reconstructed image. In this way, the solution can be defined as the function minimizing the discrepancy functional

$$\min_{T' \in E'} \|GT' - V'\|^2 \quad (15)$$

Subject to the constraint

$$(I - R_H)T' = 0 \quad (16)$$

where $R_H = R^T R$ is the projection operator onto the subspace E'' of the E' object space. The constraint of Equation (16) can be written $T' = R^T T''$. By Equation (16), Equation (15) can be rewritten as

$$\min_{T'' \in E''} \|YT'' - V'\|^2 \quad (17)$$

where $Y = GR^T$. The dimensions of system response matrix are reduced from $G(M \times P)$ to $Y(M \times Q)$, indicating that the condition number of system response matrix can be reduced in the numerical analysis point of view. Moreover, with the aid of regularization method [15], the desired solution can be expressed as the minimization of the following weighted sum of the residual norm and the side constraint

$$\min_{T'' \in E''} J(T'') = \|YT'' - V'\|^2 + \mu \|LT''\|^2 \quad (18)$$

where L is the regularization matrix, which controls the smoothness of the desired solution. In order to preserve the reconstructed image edges, the derivative operator is chosen in this paper. The regularization parameter $\mu \geq 0$ controls the weight given to minimization of the side constraint relative to minimization of the residual norm. It controls the sensitivity of the regularized solution to the measurement errors in G and V . Thus the regularization parameter is very crucial and should be chosen with care. There are numerous optimization methods to compute the optimal μ . In this paper, the Generalized Cross-Validation (GCV) method is used to ensure sufficient reconstruction accuracy [16].

3. SIMULATION AND ANALYSIS

Numerical simulations have been performed to validate the feasibility of the proposed image reconstruction algorithm. A simulation model based on the BHU-2D-U has been established. As is shown in Figure 2, the BHU-2D-U consists of 48 receiving antennas/elements and they are installed on a plane in U-shaped geometry. There are three arms in the array, including two horizontal arms and one vertical arm. The horizontal arm contains 12 receiving antennas and the spacing between antennas is 2.62λ ($\lambda = 8.824\text{mm}$), while the vertical arm contains 24 receiving antennas and the spacing between adjacent antennas is 1.46λ . The sampling spacing does not meet the Nyquist Theorem, aliasing error will be introduced in the BHU-2D-U. Thus, background cancelation technique is used to reduce the influence of aliasing error.

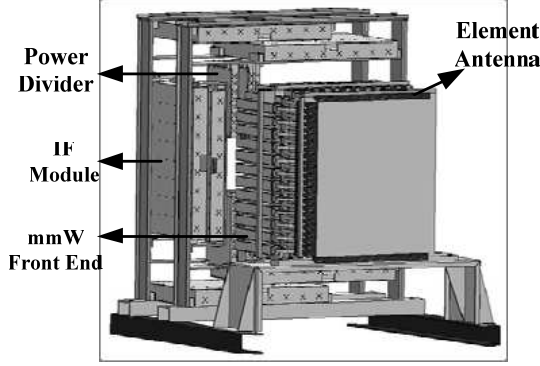


Figure 2. Antenna array of BHU-2D-U.

Referring to the definition of far- and near-fields of antenna array [7].

$$\begin{cases} R_{f1} \geq 2\frac{D^2}{\lambda} & \text{general far-field} \\ R_{f2} \geq 20\frac{D^2}{\lambda} & \text{absolute far-field} \end{cases} \quad (19)$$

where D denotes the dimension of antenna array. The general far-field of BHU-2D is 39.1 m, which is far beyond the actual imaging distance.

The original scene brightness temperature distribution is shown in Figure 3. The brightness temperature is 280 K for human body, 0 K for the background and 150 K for the weapon. The imaging distance is set as 3 m and the FOV is $1 \text{ m} \times 2 \text{ m}$.

Assuming the rectangular pre-detection filters are used prior to correlation, the measurement noise ΔV due to the limited integration time can be expressed as [17]

$$\begin{aligned} \sigma_{r,i}^2 = & \frac{1}{2B\tau_{eff}} \left\{ (T_A + T_R)^2 \left[1 + \Lambda \left(\frac{2\Delta f}{B} \right) \right] \right. \\ & \left. + V_{r,i}^2(u, v) \left[1 + \Lambda \left(\frac{2\Delta f}{B} \right) \right] - V_{i,r}^2(u, v) \left[1 - \Lambda \left(\frac{2\Delta f}{B} \right) \right] \right\} \quad (20) \end{aligned}$$

where $\Lambda(x) = 1 - |x|$ for $|x| \leq 1$ and 0 elsewhere, T_A is the brightness temperature of the scene, T_R the receiver noise temperature, τ the equivalent integration time, $\Delta f = f_o - f_{LO}$ the difference between the filter's central frequency and local oscillator's frequency, and B the noise bandwidth. In this model, the simulation parameters based on BHU-2D-U are set as: $B = 400 \text{ MHz}$ and $\Lambda(2\Delta f/B) = 0$ since the double side band receiver is employed. When the integration time is set

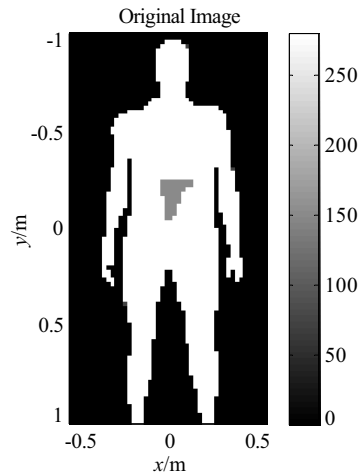


Figure 3. Original scene of simulation.

as 0.5 second, the signal to noise ratio of measured visibility function is about 34.1 dB. Under this condition, the images are reconstructed by the direct Fourier method, corrected Fourier method, Moore-Penrose pseudo inverse method. The corresponding simulation results are shown in Figures 4(a)–(c). For the proposed method, the information of target is approximated by the image reconstructed by corrected Fourier method, as shown in Figure 4(e). By employing the R operator, the dimension of unknown solutions is remarkably reduce from 4608 to 2214. In this way, the image result by proposed regularization method is shown in Figure 4(d). The cross-sections of these reconstructed images at the plane ($y = -0.14$ m) are illustrated in Figure 5.

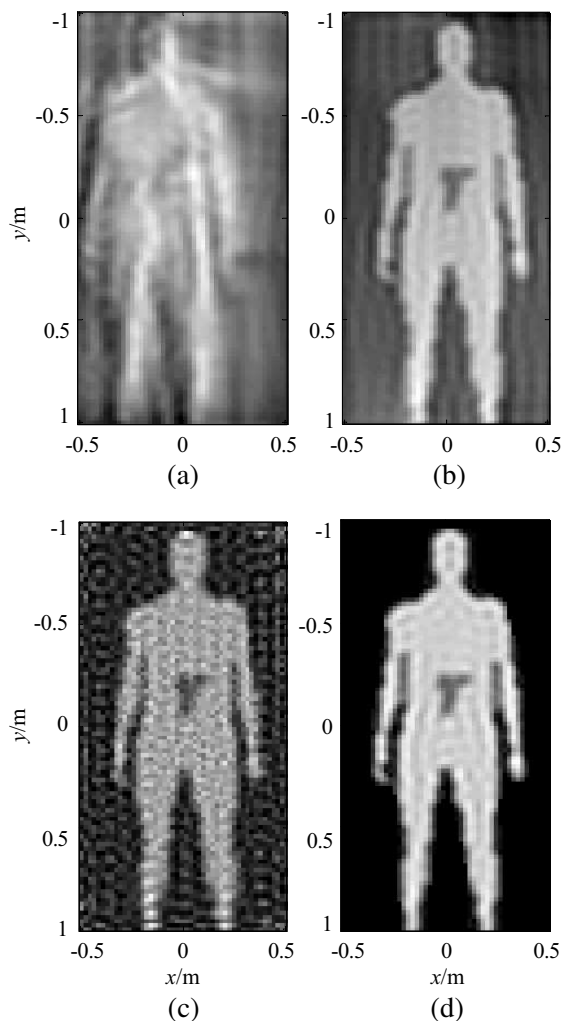
To compare the results of these imaging methods objectively, their root-mean square error (RMSE) can be calculated as

$$RMSE(X_1, X_0) = \sqrt{\sum_p \sum_q |X_1 - X_0|^2} / \sqrt{\sum_p \sum_q |X_0|^2} \quad (21)$$

where X_0 is the original image and X_1 the reconstructed image. The RMSE for different reconstructed images are given as: 0.56 for direct Fourier method, 0.27 for corrected Fourier method, 0.29 for Moore-Penrose pseudo method and 0.16 for the proposed regularization method. It reveals that the direct Fourier method is invalidated in the near-field case. The corrected Fourier method has a better performance than the direct method, but still produces unacceptable errors. In this simulation, the condition number of G is $c(G) \approx 2 \times 10^3$ that indicates

highly ill condition problem. Hence, the Moore-Penrose pseudo method is sensitive to the measurement errors. In the proposed regularization method, the dimensions of matrix Y are reduced to 1128×2214 , and the condition number of Y is significantly reduced to $c(Y) \approx 800$. Thus, the image reconstructed by the proposed method is more accurate than the results of the other methods. The regularization parameter computed by the GCV method is about 4.9.

In the above analysis, the targets temperature distribution is accurately approximated by a focal plane with imaging distance. However, the focusing approximation errors are inevitable in the



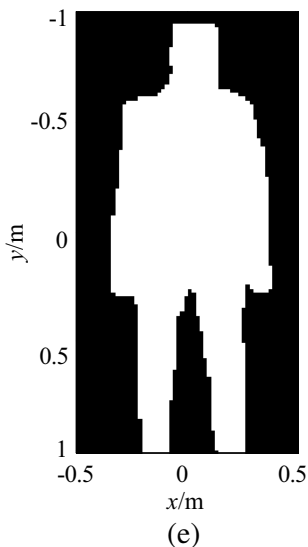


Figure 4. Images reconstructed by (a) direct Fourier method, (b) corrected Fourier method, (c) Moore-Penrose pseudo inverse method, (d) the proposed regularization method, (e) the lineament of the target.

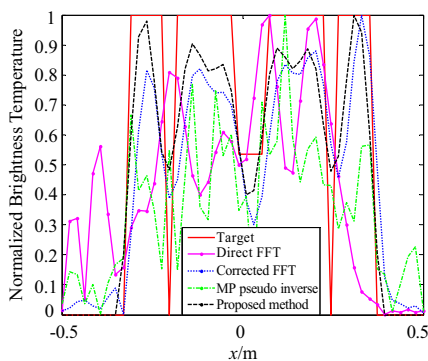


Figure 5. Cross-section ($y = -0.14$ m) of the results.

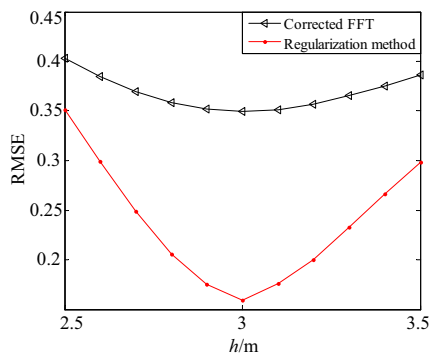


Figure 6. RMSE caused by the focusing error.

practical imaging system. In order to analyze the influence of the focusing error on the reconstructed image, numerical simulations are performed. Supposed the focusing distance changing from 2.5 m to 3.5 m and the focusing error Δh $[-0.5$ m, 0.5 m], the simulation results of the RMSE are shown in Figure 6.

From Figure 6, we can see that the image error reconstructed by the regularization method is well below to the corrected Fourier method and the reconstruction error is proportional to the focusing error. Since the Moore-Penrose pseudo method is extremely sensitive to focusing error, the RMSE is too high to be shown in the same figure. Moreover, the simulation results indicate that the proposed regularization method is insensitive to the focusing error.

4. EXPERIMENTAL RESULTS

In order to demonstrate the proposed image reconstruction algorithm, near-field imaging experiments on a person are carried out with the BHU-2D-U instrument. Before the imaging experiment, the system response G matrix of BHU-2D-U is measured. Each column of G can be approximated by the corresponding one of point spread functions (PSFs) within the FOV [10].

$$G_{M \times i} = V'_{M \times 1} = G_{M \times P} \cdot T'_i \quad (22)$$

where T'_i denotes that the point source is located at the (i) -th pixel in the FOV with specific focusing distance, $G_{M \times i}$ is the corresponding measured PSF. In the experiments, the point source consists of a noise diode, an amplifier and a pyramid horn antenna. It is installed on a mechanical scanner. All of the PSFs within the whole FOV can be measured with the aid of the mechanical scanner. It should be ensured that the point source is stable throughout the measurements. The point source is also switched off at each point to provide a measure of background and systematic bias, which are used to reduce the influences of aliasing error and system offset according to Equation (10). In the measurements, limited by the size of mechanical scanner, the focusing distance is set as 2.5 m, the sizes of scanning FOV are 70 cm \times 80 cm and the number of scanning points is 52 \times 41. Hence the dimensions of measured G matrix are 1128 \times 2132. The integration time in experiment is 0.5 s. In the case, The measured results shown that the condition number of G is $c(G) \approx 3.22 \times 10^4$.

Imaging experiments on a person with concealed weapon are carried out. In order to form a uniform background, a metal plane with 45° incline to the ground is fixed behind the target. The plane can reflect the spontaneous radiation from the sky and form a uniform cold background. The integration time in the experiment is also set to 0.5 s. In order to further investigate the posedness of the measured near-field visibility equations, the Picard's rule is applied [18]. Using the SVD,

it is easy to show the solution of Equation (10) can be obtained

$$T' = \sum_{i=1}^n \frac{u_i^T V'}{\sigma_i} v_i \tag{23}$$

where u_i , v_i and σ_i are the UV decomposition vectors and singular value of G . According to the Picard's rule, when the descending speed of the Fourier coefficients $u_i^T V'$ is faster than the singular value σ_i , it is a well-posed problem and the solution will be convergent. On the contrary, when the descending speeds of $u_i^T V'$ is lower than σ_i , the problem is ill-posed and the solution appears completely random. Based on the imaging experiment on a human body, the Picard condition of near-field visibility equations is shown in Figure 7. We can see that the Picard condition is untenable and the inverse problem is indeed not well-posed for the near-field imaging in BHU-2D-U.

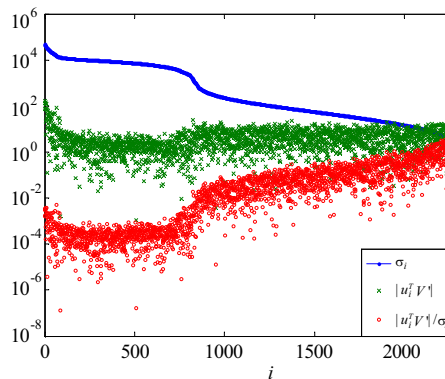


Figure 7. Picard diagram of near-field visibility equations.

In this case, the problem must be regularized in order to provide a unique and stable solution. Based on the proposed regularization method, the dimensions of Y is reduced to 1128×1261 from $G(1128 \times 3456)$, with $c(Y) \approx 3 \times 10^3$. The imaging result is shown in Figure 8(a). Figure 8(c) illustrates the corresponding photograph captured by an optical camera, in which a small metal plate is held in the person's hand. The metal plate can be recognized clearly from the mmW image, although it is concealed under his shirt. Here, the optimal regularization parameter is about 122 by means of GCV method To compare the performance of the imaging algorithms, the imaging result based on the corrected Fourier method is shown in Figure 8(b). Clearly, we can see that the image reconstructed by the proposed regularization method is better than the corrected Fourier

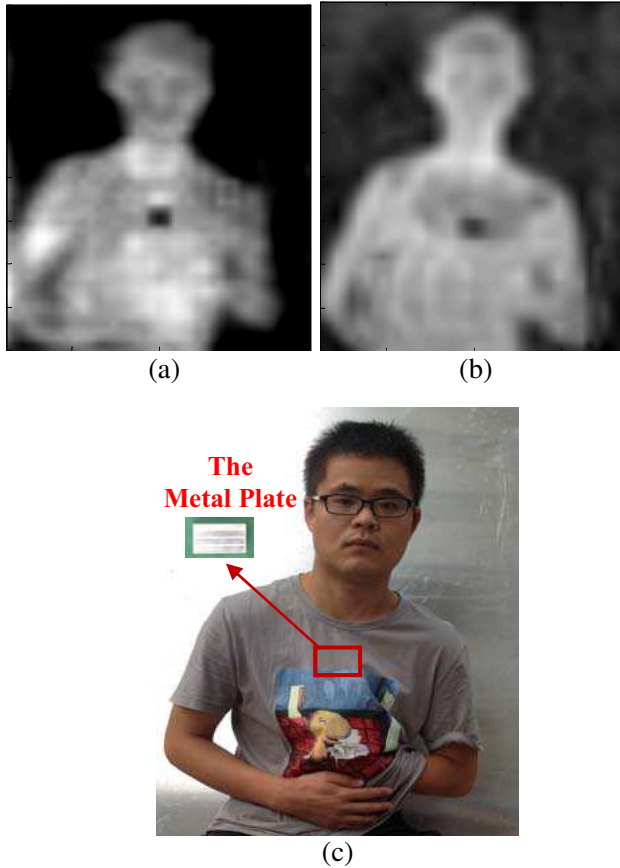


Figure 8. (a) Imaging result of proposed regularization method, (b) imaging result of corrected Fourier method, (c) photograph of a person with concealed metal plate.

method. The perturbations are significantly suppressed and the image of concealed metal plate is more clearly than the corrected Fourier method.

5. CONCLUSION

In this paper, the near-field imaging problem for millimeter-wave SAIR has been analyzed. For accurate image reconstruction, a numerical image reconstruction algorithm has been proposed. The method is more suitable for the case, when large number of antenna arrays

and large FOV are applied. By employing this proposed numerical method, the accuracy and stability of the reconstructed image can be significantly improved in the presence of measurement noise and focusing error. Numerical simulations have been performed to validate the proposed numerical algorithm. The simulation results demonstrate the advantages of this regularization method over existing corrected Fourier method and Moore-Penrose pseudo inverse method. Finally, the imaging experiments on a person are conducted for BHU-2D-U. The results show that the feasibility of the proposed method in practical millimeter-wave SAIR.

REFERENCES

1. Wikner, D. A., "Progress in millimeter-wave imaging," *Proc. SPIE*, Vol. 7936, 79360D, Feb. 10, 2011.
2. Kolinko, V. G., S. Lin, A. Shek, W. Manning, C. Martin, M. Hall, O. Kirsten, J. Moore, and D. A. Wikner, "A passive millimeter-wave imaging system for concealed weapons and explosives detection," *Proc. SPIE*, Vol. 5781, 85–92, May 19, 2005.
3. Lovberg, J. A., C. Martin, and V. G. Kolinko, "Video-rate passive millimeter-wave imaging using phased arrays," *Proc. MWSYM*, 1689–1692, Honolulu, HI, Jun. 3–8, 2007.
4. Huang, J. and T. Gan, "A novel millimeter wave synthetic aperture radiometer passive imaging system," *Proc. ICMMT*, 414–417, Aug. 18–21, 2004.
5. Zheng, C., X. Yao, A. Hu, and J. Miao, "A passive millimeter-wave imager used for concealed weapon detection," *Progress In Electromagnetics Research B*, Vol. 46, 379–397, 2013.
6. Zheng, C., X. Yao, A. Hu, and J. Miao, "Initial results of a passive millimeter-wave imager used for concealed weapon detection BHU-2D-U," *Progress In Electromagnetics Research C*, Vol. 43, 151–163, 2013.
7. Laursen, B. and N. Skou, "Synthetic aperture radiometry evaluated by a two-channel demonstration model," *IEEE Trans. Geosci. Remote Sens.*, Vol. 36, No. 3, 822–832, May 1998.
8. Duffo, N., I. Corbella, and F. Torres, "Advantages and drawbacks of near field characterization of large aperture synthesis radiometers," *Proc IEEE Microrad*, Rome, Italy, 2004.
9. Tanner, A. B., B. H. Lambrigsten, T. M. Gaier, and F. Torres, "Near field characterization of the GeoSTAR demonstrator," *Proc. IGARSS*, 2529–2532, Jul. 31, 2006.
10. Tanner, A. B. and C. T. Swift, "Calibration of a synthetic aperture

- radiometer,” *IEEE Trans. Geosci. Remote Sens.*, Vol. 31, 257–267, 1993.
11. Zhang, C., J. Wu, H. Liu, and J. Yan, “Imaging algorithm for synthetic aperture interferometric radiometer in near field,” *Science China Technological Sciences*, Vol. 54, 2224–2231, 2011.
 12. Anterrieu, E., “A resolving matrix approach for synthetic aperture imaging radiometers,” *IEEE Trans. Geosci. Remote Sens.*, Vol. 42, No. 8, 1649–1656, Aug. 2004.
 13. Bertero, M. and P. Boccacci, *Introduction to Inverse Problems in Imaging*, Instit. Phys., London, UK, 1998.
 14. Peichel, M., H. Suess, and M. Suess, “Microwave imaging of the brightness temperature distribution of extended areas in the near and far field using two-dimensional aperture synthesis with high spatial resolution,” *Radio Science*, Vol. 33, No. 3, 781–801, 1998.
 15. Tikhonov, A. and V. Y. Arseninn, *Solution of Ill-posed Problems*, John Wiley & Sons, New York, 1977.
 16. Golub, G. H., M. Heath, and G. Wahba, “Generalized cross validation as a method for choosing a good ridge parameter,” *Technometrics*, Vol. 21, 215–223, 1979.
 17. Ruf, C. S., C. T. Swift, A. B. Tanner, and D. M. Le Vine, “Interferometric synthetic aperture microwave radiometry for the remote sensing of the earth,” *IEEE Trans. Geosci. Remote Sens.*, Vol. 26, 597–611, 1988.
 18. Hansen, C., “The discrete Picard condition for discrete ill-posed problems,” *BIT Numerical Mathematics*, Vol. 30, No. 4, 658–672, 1990.